2020

Unique growth pathway in solution–solid–solid nanowires: Cubic to hexagonal phase transformation

Yi-Hsin Liu

Ho-Ying Chen

Hsiu-Fang Fan

Yu-Hsien Chen

Fudong Wang

ACS OMEGA

http://pubs.acs.org/journal/acsodf

Article

Unique Growth Pathway in Solution–Solid–Solid Nanowires: Cubic to Hexagonal Phase Transformation

Yi-Hsin Liu,* Ho-Ying Chen, Hsiu-Fang Fan, Yu-Hsien Chen, and Fudong Wang

Cite This: *ACS Omega* 2020, 5, 18441–18448

Read Online

ACCESS | Metrics & More | Article Recommendations | Supporting Information

ABSTRACT: Solution–solid–solid (SSS) nanowires can be catalyzed by superionic Ag_2S *via* ion diffusion. Here, we synthesize ZnS nanowires of the wurtzite crystal structure and heterostructures *via* a low-temperature growth pathway. Single-crystalline ZnS nanowires were produced by varying reaction time and temperature (120–200 °C) *via* thermal decomposition of a single-source precursor, $Zn(DDTC)_2$. A phase transformation (zinc blende → wurtzite) was observed during the synthesis with a three-step growth pathway proposed. Temperature-controlled phase transformation facilitates oriented attachment into a 1D nanowire, followed by helical epitaxial and lateral growths during ripening. Additionally, the CdS–ZnS heterostructured nanowires can be obtained after introducing the $Cd(DDTC)_2$ precursor. ZnS nanowires of defined diameters (5–10 nm) are served as backbones to grow heterostructures of ternary semiconductors with multicolor photoluminescence (450–800 nm). Structural and optical characterizations (PL, 2D PLE, and TCSPC) are investigated to confirm origins of broadband emission from multiple lifetimes (0.5–12 ns) for exciton recombination in heterostructures. Our study demonstrates this unique growth pathway for SSS nanowire synthesis under mild, facile, and atmospheric conditions.

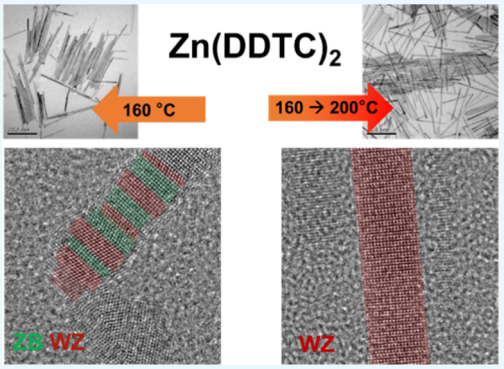

INTRODUCTION

Various nanoparticles have been employed to grow nanowires in three major synthesis conditions. Among all, vapor–liquid–solid (VLS)[1−5] and solution–liquid–solid (SLS)[6−10] methods are well studied while the solution–solid–solid (SSS) pathway is still under investigation.[11−13] VLS methods (>650 °C) produce large-diameter nanowires because of catalyst agglomeration at high temperature.[13,14] Alternatively, colloidal solution processes, SLS (250–320 °C) and SSS (<250 °C), tentatively grow uniform nanowires by activating precursor activity *via* capping ligands, solvent types, and catalysts at low temperature.[15,16] Especially, catalysts of modulated sizes, surface energy, and chemical compositions affect phases, shapes, and diameters of nanowires.[17−20] Previously, Wang and co-workers have demonstrated one unique example of growing straight, bright, and nearly pure-phase CdTe nanowires through a solution process under mild reaction conditions (<240 °C).[14,20,21] These pure-phase CdTe nanowires can be catalyzed by solid-state $Bi_xCd_yTe_z$ nanoparticles that have intrinsic defects and nonstoichiometric lattice phases.[20]

Superionic conductors (SICs), including silver- or copper (I)-based chalcogenides (Ag_2S, Ag_2Se, and Cu_2S), have been reported for nanowire growth *via* structural defect vacancy.[13] The Ag_2Se crystal structure has defects in two known phases, orthorhombic (β) and cubic (α), which rationally catalyze nanowire growths.[22] With utilization of the Ag_2Se nanoparticles, ultralong MnSe nanowires with defined diameters (~35 nm) and extended length dimensions (>5 μm) were produced by employing $MnCl_2$, $(PhCH_2)_2Se_2$, and silver catalysts (Ag^+/Mn^{2+} = 0.3%) at 120–220 °C. As far, Ag_2Se has been demonstrated as a model in growing high-quality SSS-catalyzed nanowires because of a small mismatch (2.40%) between zinc blende (ZB) MnSe(011) and *bbc*-Ag_2Se(211).[11]

Other SIC catalysts, such as Ag_2S, also initiate nanowire growth in a moderate temperature range (100–200 °C). Presynthesized Ag_2S nanoparticles have been employed to grow various 1D semiconductors (ZnS,[23,24] CdS,[24,25] $CuInS_2$,[26] $AgInS_2$,[23] and $AgInZn_7S_9$[27]). Solution processes are facile methods to prepare colloidal nanowires with uniform diameters and shapes. Additionally, nanowire growths can be accompanied with catalyst formation in a one pot for scalable purpose.[28−30] To this end, controls of diameters and crystallinity are the current challenges for sulfide-based nanowires.

In this study, high-quality wurtzite (WZ) ZnS nanowires with uniform diameters (5.9 ± 0.7 nm) were reported *via* a structural transformation. These ZnS nanowires can be facilely

Received: May 17, 2020
Accepted: July 6, 2020
Published: July 17, 2020

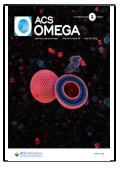

https://dx.doi.org/10.1021/acsomega.0c02302
ACS Omega 2020, 5, 18441–18448

prepared *via* thermal decomposition of zinc single-source precursor under an ambient conduction. ZnS is selected because of its wide band gaps for UV pumping (3.7−3.8 eV in the WZ structure)[31−33] at heterojunctions or intrinsic surface traps.[13,32,34] Additionally, ZnS nanowires are also served as active backbones to grow 1D heterostructures with broadband emissions.[35,36] In this work, synchrotron-based characterizations from atomic scales to solid states were rationally conducted to study SSS-synthesis pathways in detail.

RESULTS AND DISCUSSION

Morphology Control. Crystalline ZnS nanowires with a nearly pure WZ phase were conducted *via* SSS synthesis (Figure 1a). High-resolution transmission electron microscopy

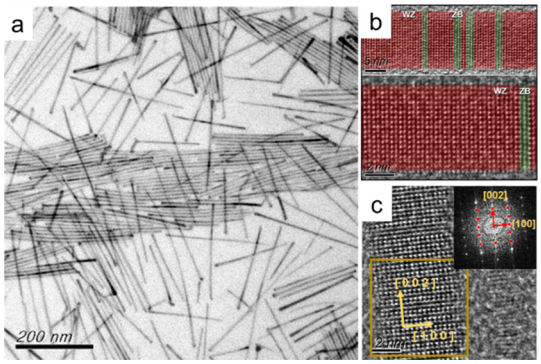

Figure 1. (a) Representative TEM image of ZnS nanowires, (b) HRTEM images of a ZnS nanowire composed of major WZ with little ZB, and (c) top-view HRTEM image with FFT inset showing two lattice directions, [002] and [100].

(HRTEM) images and fast Fourier transforms (FFTs) suggest [002] as the major growth direction in the WZ structure with small lattice alternation (Figure 1b,c). The alternation between WZ and ZB structures has been commonly observed in VLS-, SLS-, and SSS-catalyzed nanowires. Nearly pure-WZ CdTe nanowires were only reported in the use of solid-state nanoparticles *via* SSS synthesis (<250 °C).[20] Given that both ZB and WZ have similar surface energy (0.58−0.62 J/m^2),[37] as high reaction temperature induces rapid crystal nucleation and lattice growth, the lattice alternation between ZB and WZ is commonly observed. By lowering reaction temperature, the surface energy-optimized WZ structure may be achieved with less stacking faults and phase alternations.

It is noteworthy that reaction temperature affects the nanowire morphology. Various temperature syntheses are employed to grow ZnS nanowires with different diameters. In Figure 2, type-A nanowires refer to a synthesis conducted at single reaction temperature (a: 160, c: 200 °C) while type-B nanowires refer to the synthesis conducted at two temperatures (b: 160 → 200 °C). Surprisingly, narrow diameter distributions (only 13%) for type-B nanowires suggest optimized synthesis conditions. The type-B nanowire synthesis involves lower decomposition temperature (160 °C) and then higher growth temperature (200 °C) for the straight 1D morphology. Two types of nanowires with indistinguishable FFT patterns suggest identical growth orientation. Remarkably, the type-B nanowires also reveal the nearly pure WZ crystal structure and straight morphology. All nanowires were investigated by UV−vis absorption as well as synchrotron-based X-ray diffraction (XRD) and extended X-ray absorption

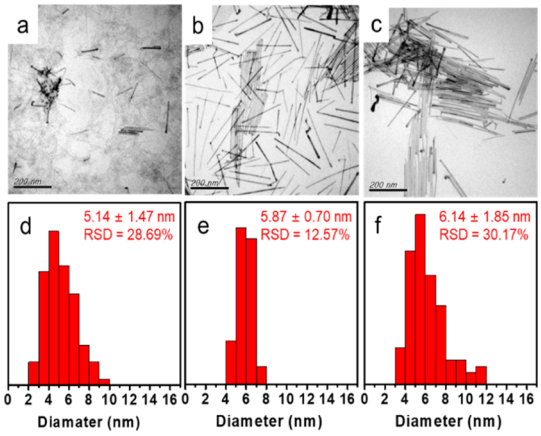

Figure 2. Representative TEM images and diameter analyses of (a,d) type-A ZnS nanowires synthesized at 160 °C for 30 min (5.14 ± 29%), (b,e) type-B ZnS nanowires synthesized at 160 °C for 15 min and then 200 °C for 15 min (5.87 ± 13%), and (c,f) type-A ZnS nanowires synthesized at 200 °C for 30 min (6.14 ± 30%). The diameter statistics of (d−f) are based on 100 measurements of individual nanowires.

fine structure (EXAFS). On the merits of pure structure and straight morphology,[38] the type-B nanowires with uniform diameters (5.9 ± 0.7 nm) are targeted for scalable synthesis.

Epitaxy Growth. To study crystal structures of ZnS nanowires and Ag_2S catalysts, various characterization techniques [XRD, TEM, HRTEM, and scanning TEM (STEM) with high-angle annular dark-field−energy-dispersive X-ray spectroscopy (HAADF−EDS) mapping] were performed. XRD and HRTEM confirm the WZ structure as the major crystal phase in ZnS nanowires. Their XRD patterns remain identical after annealing to different temperatures (120, 160, and 200 °C, Figure S10), suggestive of no structure change after the synthesis. The relatively sharper (002) feature indicates the long crystalline domains, similar to the observed lengths in TEM (>200 nm). Based on synthesis results at 120, 160, and 200 °C, ZnS nanowires can be catalyzed by cubic Ag_2S (argentite) above 173 °C as well as monoclinic Ag_2S (acanthite) even below 173 °C. Elemental mappings in HAADF−EDS reveal Zn signals uniformly distributed in nanowires while Ag signals are shown at the tip only (Figure S11). Because of small sizes of Ag_2S nanoparticles (<5 nm), their diffraction patterns cannot be identified.

HRTEM and FFT were employed to reveal the crystal structure of Ag_2S nanoparticles (Figures S12−S15). Three lattice fringes of *d*-spacing (2.238, 2.426, and 2.371 Å) are assigned to three directions ([031], [013], and [−103]) in the α-Ag_2S phase. Based on the spatial directions and geometry, the [131] direction at the catalyst−nanowire interface is proposed. The lattice *d*-spacing of ZnS(110) and Ag_2S(131) is very close (1.911 *vs* 1.918 Å). With the small lattice mismatch (0.36%) and high spatial correlation, epitaxy growth of nanowire (110) to catalyst nanoparticle (131) facets is thus proposed for SSS-catalyzed ZnS nanowires.[11,39]

Diameter Controls. Diameter controls of ZnS nanowires were studied by varying reaction temperatures (120, 160, and 200 °C) and time. At 120 °C, after the first 60 min, no nanowire but only cluster aggregates were found in TEM. At higher temperature (160, 200 °C), tapered ZnS nanowires with enlarged diameters of 5.95 nm (±24%) and 6.14 nm (±30%) were obtained. Diameters of these nanowires were

https://dx.doi.org/10.1021/acsomega.0c02302
ACS Omega 2020, 5, 18441−18448

slightly beyond quantum confinement regimes of ZnS (two times of Bohr radius, 2.5 nm). Thus, all excitonic features were reasonably similar (317 nm, 3.91 eV after peak and background deconvolution). Although UV−vis absorption was unable to distinguish diameter variations, evolution of ZnS nanowire growths can be conducted by electron microscopy and other X-ray techniques.

Based on XRD results, diameter development with a phase transformation is proposed. The initial cluster aggregates of ZB structure were gradually consumed during the nanowire growth and eventually disappeared in the final products. To better understand the growth process from the aggregates to the nanowires, the reaction temperature was further lowered to 120 °C with kinetic studies (0.5−3 h). Structural characterizations (TEM, EXAFS, and XRD) are employed to reveal such unusual growth phenomenon. In Figure 3, ZnS nanowires

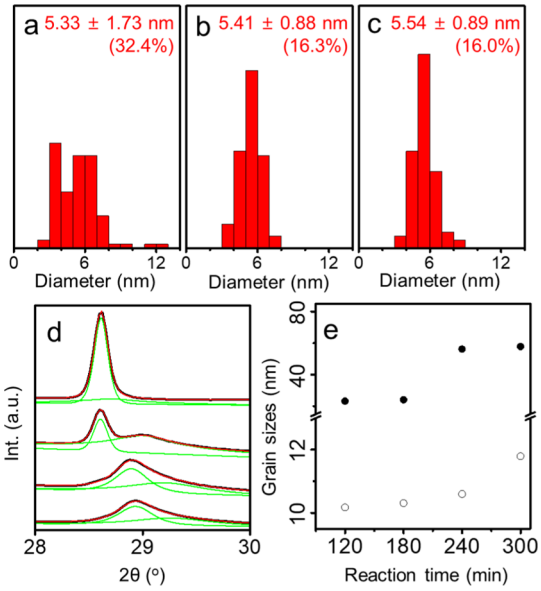

Figure 3. Statistic TEM diameter analysis of ZnS nanowires synthesized at 120 °C after (a) 180, (b) 240, (c) and 300 min. (d) XRD patterns with deconvoluted profiles of ZnS nanowires after 120, 180, 240, and 300 min (bottom to upper). (e) Grain-size development along $[002]_{WZ}$ (dots) and $[111]_{ZB}$ (circle) directions. The diameter statistics of (a−c) are based on 100 measurements of individual nanowires.

synthesized at 120 °C (180, 240, and 300 min) show a diameter development of 5.33 nm (±32%), 5.41 nm (±16%), and 5.54 nm (±16%). Similarly, ZnS nanowires synthesized at 160 °C (30, 60, 120, and 180 min) also show a noticeable diameter enlargement of 5.14 (±29%), 5.95 (±24%), 6.18 (±29%), and 7.03 nm (±28%), as shown in Figure S25. These TEM results clearly demonstrate effects of temperature and time for ZnS nanowire growths.

Alternatively, the diameter enlargement (lateral thickening) is also suggested in XRD. From peak deconvolution *via* Gaussian profiles and Scherrer equation fitting (Figure 3d), developments of *d*-spacing and grain sizes in several mixed phases (WZ_{110}, WZ_{100}, WZ_{002}, and ZB_{111}) are qualitatively and quantitatively separated. At 120 °C, the grain-size development for $[002]_{WZ}$ and $[111]_{ZB}$ was noted during nanowire growth (22 → 58 nm, 10 → 12 nm, Figure 3e). The enlarged and increased lattice domains suggest aggregation of ZB domains, followed by oriented attachment with phase transformation.[40]

At 160 °C, noticeable diameter enlargement in lateral directions ($[100]_{WZ}$, $[110]_{WZ}$) was observed (3.2 → 6.7 nm, 5.0 → 7.0 nm, Table S5). The diameter enlargement phenomenon is confirmed by both XRD and TEM results, which are highly self-correlated (Figure S33d).

For reaction temperature (200 °C) above the Ag_2S superionic phase, ZnS nanowires can be still actively produced, but the morphology and diameter control are poor. Because reaction temperature (120−200 °C) in our process was not high enough to melt Ag_2S nanoparticles, the poor diameter distribution may be because of structural rearrangement upon the lateral surface, as previously reported in VLS nanowires.[41] Such tapered morphology was rarely observed in SLS nanowires.[30] It is hypothesized that competitive growth pathways (*e.g.*, classical Ostwald ripening or oriented attachment) may be actively involved toward the nanowire morphology and diameters.[42,43]

From Molecules to Nanowires. Small-angle X-ray scattering (SAXS) is a powerful technique to evaluate size, shape, and structural development of nanostructures. The presence of low-*q* features in SAXS is representative of nanostructured aggregates. When $Ag(OAc)_2$ was not introduced, two broad features in SAXS (blue area, Figure S3) suggest the presence of molecular aggregates after thermal decomposition of $Zn(DDTC)_2$, prior to nanowire formation. After $Ag(OAc)_2$ was added, emerging SAXS features were observed, as shown in Figure 4a. In the first 30 min, SAXS

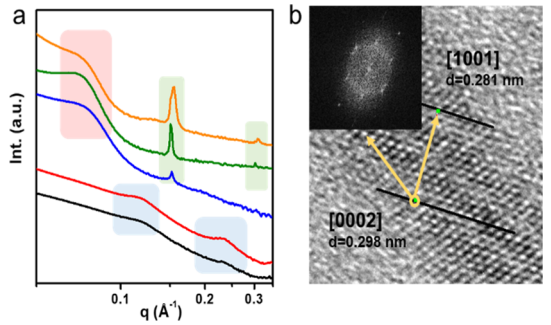

Figure 4. (a) SAXS spectrum of $Zn(DDTC)_2$ decomposed at 160 °C with $AgNO_3$ after 10 (black), 30 (red), 60 (blue), 120 (green), and 180 min (orange). (b) HRTEM image of the early-stage ZnS prenanowires showing the helical 1D morphology.

remains still (blue area). After 60 min, a low-*q* feature below 0.1 $Å^{-1}$ suggests prenanowire formation after attachment of aggregates into large nanoparticles (pink area, Figure 4a). Simultaneously, sharp SAXS features (green area) are similarly referred to ordered domains in nanowires. The lower-*q* peak (0.0704 A^{-1}, 8.9 nm) shall be correlated to lateral dimensions of nanowires (diameter and ligand length) while the higher-*q* peaks (0.1506 and 0.3022 A^{-1}) suggest structural periodicity (4.2 nm) for crystalline domains.

Interestingly, early-stage ZnS prenanowires morphologically resemble twisted ropes with tilted lattice periodicity in HRTEM (Figure 4b). The periodicity (4.2 nm) equivalent to common multiples of d_{002} (0.298 nm) as well as d_{101} (0.281 nm) in WZ suggests helical growth correlation. Formation of the prenanowires is proposed as assembled ZB aggregates *via* oriented attachment along $[100]_{ZB}$, $[010]_{ZB}$, and $[001]_{ZB}$ directions.[44] During the phase transformation, the prenanowire $(111)_{ZB}$ axis is geometrically converted to the nanowire

https://dx.doi.org/10.1021/acsomega.0c02302
ACS Omega 2020, 5, 18441−18448

$(002)_{WZ}$ axis. The growth phenomenon is also observed in CdS nanowires (Figures S21 and S23). Based on XRD, SAXS, and HRTEM results, a helical growth of SSS-catalyzed nanowires is proposed. Previously, a phase transformation from the cubic ZB to hexagonal WZ structure has been also observed in CdSe nanomaterials.[44] Direct observation of unique periodic patterns (SAXS) and helical morphology (HRTEM) is first reported in 1D nanowires.

EXAFS technique reveals chemical environment changes for nanowire growths. Based on EXAFS fitting results, the zinc site in $Zn(DDTC)_2$(s) is surrounded by four sulfur atoms (2.367 Å) in the first shell and another sulfur atom in the second shell (2.710 Å). Upon dissolving in amine solution, increasing Zn−N with decreasing Zn−S components suggests formation of amine-substituted complexes (Figure S1). Upon thermal decomposition (120, 160, and 200 °C), additional Zn−Zn components indicate aggregate formation. During growths, coordination numbers (N_{Zn-S}) and atom-to-atom distance (R_{Zn-S}) are varied in time and temperature accordingly. Information of N_{Zn-S} and R_{Zn-S}, as shown in Table S6 and Figure S39, together with ZB−WZ transformation and diameter growths suggests a kinetic growth pathway from molecules to nanowires.

Growth Pathway. According to diameters, coherent length, and coordination changes (TEM, XRD, and EXAFS), a three-stage growth pathway is proposed as length growth (I), diameter thickening (II), and diameter ripening (III), as shown in Scheme 1. The stage (I) starts after introduction of Ag^+ and

Scheme 1. Proposed Growth Pathway for SSS-Catalyzed ZnS Nanowires

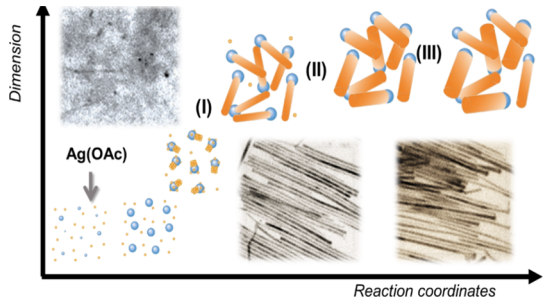

ends as prenanowires observed in TEM. At 120 °C, the stage (I) takes 120−180 min to complete. At 160 and 200 °C, the stage (I) periods are reduced to 30−60 and 5−10 min only. In the stage (I), XRD features are very board, indicative of small crystals in the prenanowires. It is also noteworthy that ZB is the primary crystal structure in this stage. As the $(111)_{ZB}$ peak becomes sharper and more intense, the prenanowires gradually become longer. At the end of the stage (I), mixed phases of $(111)_{ZB}$, $(100)_{WZ}$, and $(110)_{WZ}$ peaks are observed, suggestive of a gradual transformation from ZB to WZ during ripening.

In the stage (II), lateral growths and narrow diameter distribution are representative features while ZB−WZ transformation still continues. It is known that surface ligands affect the nanowire morphology and crystal structure. Natural donor ligands (L-type),[45] such as oleylamine, have been used for nanowire synthesis.[44,46] According to the surface energy calculation, the amine-passivated surface may lower work functions for nonpolar facets,[47,48] resulting the lowest surface energy (0.62 and 0.58 J/m^2) for individual $\{110\}_{ZB}$ and $\{11-20\}_{WZ}$ surface.[37] Thus, the crystal structure of rods and wires can be WZ, ZB, or mixed phases as their surface is passivated by amine ligands. It is rationally proposed that uncommon lateral growth may be add-on results of eliminating surface defects during ZB−WZ transformation. By the end of stage (II), the major crystal structure gradually becomes WZ. Narrow relative standard deviation (RSD) of diameters is also indicative of obtaining uniform nanowires. For the purpose of obtaining pure-phase uniform nanowires, reaction temperature in stage (II) may be raised (*e.g.*, 200 °C, like type-B nanowires) to the expedite stage (II) process.

At the very end of the stage (II) and beginning of the stage (III), some tapered nanowires were found in TEM. Based on XRD fittings, grain sizes of lateral $(100)_{WZ}$ and $(110)_{WZ}$ continue to increase, but grain sizes of axial $(002)_{WZ}$ and $(111)_{ZB}$ slightly decrease. Enlargement of lateral crystalline domains results in board diameter distributions (RSD) for the stage (III). XRD further confirms that the lateral growths actively occur along [100] and [110] directions. However, such a lateral growth in the stage (III) should be avoided for uniform diameter purpose. We propose the three-step growth pathway to reveal synergistic effects of reaction temperature and time. It also confirms the synthesis condition parameters for the type-B nanowires, which were initiated at 160 °C in the stage (I) and raised to 200 °C in the stage (II).

Ag_2S−CdS−ZnS Heteronanowires. The as-synthesized ZnS nanowires are nonemissive. However, optical properties may be enhanced *via* chemical engineering into heterostructures.[49] Two types of ZnS nanowires capped with Ag_2S tips can be utilized as backbones to grow heterostructured nanowires in a one-pot reaction. As the $Cd(DDTC)_2$ precursor is sensitive to thermal decomposition, the reaction temperature for CdS segment growths must be lowered to 100 °C prior to introduction of $Cd(DDTC)_2$−oleylamine aliquots. This injection step can be repeated several times to increase Cd-to-Zn molar ratios (0.04−0.20). After successive delivery of Cd precursors, the heterostructured nanowires were obtained. Characteristic identifications, such as XRD feature (*ca.* 44°), UV−vis (*ca.* 490 nm), and cane-like shapes in TEM images, together indicate formation of Ag_2S−CdS−ZnS heteronanowires instead of nanowire mixtures. Catalysts of Ag_2S nanoparticles remained undetectable in XRD but clearly evidenced in HRTEM images (Figure S51).

Ternary ZnS−CdS−Ag_2S (backbones, segments, and tips) nanowires can be also identified in STEM and EDS mapping (Figures 5, S52). The cane-like morphology confirms attachments of CdS segments onto ZnS backbones, likewise SLS-catalyzed heterostructured nanowires.[9] Similar diameters between ZnS nanowires and CdS segments indicate the consecutive growth by the same Ag_2S tips. It is known that lattice mismatch between ZnS(110) and CdS(103) is small

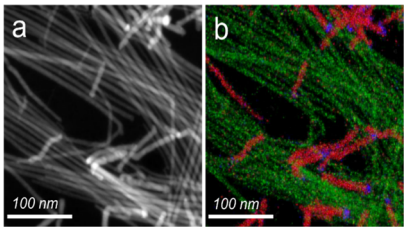

Figure 5. (a) Dark-field STEM image and (b) EDS mapping with Ag (blue), Cd (red), and Zn (green) elements for Ag_2S−CdS−ZnS heteronanowires.

https://dx.doi.org/10.1021/acsomega.0c02302
ACS Omega 2020, 5, 18441−18448

and confirmed by overlapping of $ZnS(110)_{WZ}$ and $CdS(103)_{WZ}$ XRD peaks (*ca.* 47.6°). Based on above XRD results (Figure S53), an epitaxy growth is thus suggested. Recurring growths of CdS segments can be repeated several times to increase the segment domains. After the growth, an emerging $(110)_{WZ}$ XRD peak (43.85°) suggests CdS lattice domains, similar to CdS/ZnS and CdS/Ag_2S nanocrystal growths.[50,51] Because there were no change in the $(002)_{WZ}$ peak at 28.66°, displacement or alloying process is excluded. The active Ag_2S tips at ZnS nanowires facilitate formations of ternary heterostructure *via* a low-temperature condition. Additionally, 2D PLE technique was performed to distinguish heterostructures from nanowire mixture.

The ternary Ag_2S−CdS−ZnS heteronanowires (Cd/Zn = 0.2) perform multicolor broadband emission between 450 and 800 nm. The emission bands can be perfectly deconvoluted into five individual profiles with peaks individually centered at 489, 508, 616, 657, and 714 nm (p_1−p_5, Figure 6a). The broadband emission can be explained by multiple exciton recombination induced by the heterostructures, rather than individual emission from nanowire mixtures. We also argue that emission profiles between pure CdS nanowires and ternary heteronanowires (*ca.* 580 *vs* 660 nm) are dissimilar. The broadband emission features of ternary heteronanowires are originated from discrete energy levels (415, 430, 440, and 450 nm, as shown in Figure S56) in PLE, which is often employed to identify SWCNTs in semiconducting mixtures.[52] The PL/PLE contour 2D plots reconfirm that exciton recombination is directly from CdS−ZnS heteronanowires, rather than from nanowire mixtures.

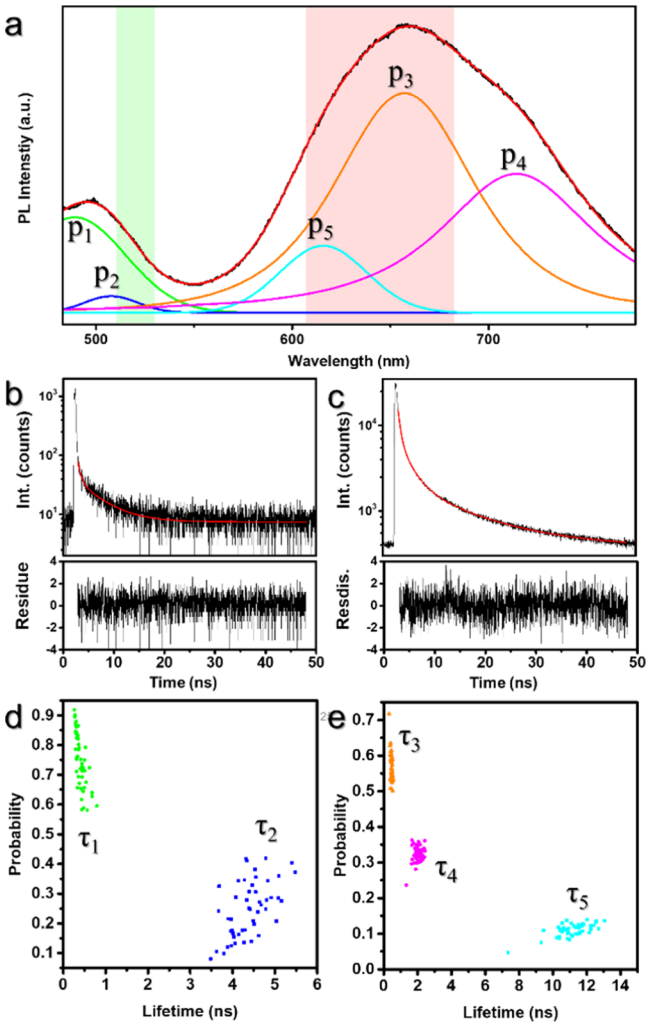

Figure 6. (a) PL of Ag_2S−CdS−ZnS nanowires with five deconvoluted peaks (p_1−p_5). Fluorescence decay spectra (upper) and intensity residues (bottom) from (b) 510−530 nm [green area in (a)] after biexponential fittings and (c) 607.5−682.5 nm [red area in (a)] after triexponential fittings. Normalized probabilities of five lifetimes, (d) τ_1, τ_2 and (e) τ_3, τ_4, τ_5, are deconvoluted from 50 individual fluorescence spots.

The broadband emission (450−800 nm) also suggests multiple radiative recombination pathways. Individual emission features have intrinsic lifetimes, spectroscopically collected by confocal imaging of nanowires spin-coated on glass slides *via* TCSPC techniques.[49] Statistics of fluorescence lifetimes (τ_1−τ_5, Figure 6d,e) *via* 405 nm excitation can be mathematically extracted from decay components in two emission regimes, 510−530 and 607.5−682.5 nm (Figure 6b,c) in using of two bandpass filters. Based on 50 individual spots of nanowire specimen on the glass slides, five exciton lifetimes (τ_1 = 0.40 ± 0.12 ns, τ_2 = 4.38 ± 0.46 ns, τ_3 = 0.45 ± 0.05 ns, τ_4 = 2.03 ± 0.23 ns, and τ_5 = 11.16 ± 0.98 ns) were extracted from microscopic emission. Relative probability (χ_i) of each lifetime was obtained after normalization (prefactor (A_i) to summation ($\sum A_i$)) in each decay.

Cross-check of ensemble PL intensity (I_{PL}) weighting and microscopic lifetime probabilities (χ_i) confirm five radiative exciton recombination pathways in two emission regimes (510−530 and 607.5−682.5 nm). The normalized probability (χ_i) matches to the weighting of ensemble I_{PL}, as listed in Table S9. Modeling of radiative recombination pathways is accordingly proposed, as shown in Figure S58. Larger probability (χ_i) and I_{PL} weighting suggest the stronger emission intensity (489 and 657 nm) with shorter lifetime ($\tau \approx 0.4$ ns). Less probability (χ_i) and I_{PL} weighting suggest the weak interband emission (508 and 714 nm) or trap state (616 nm) with much longer lifetime ($\tau > 2$ ns).[53] Multiple lifetimes indicate nature of exciton dynamics in heteronanowires.[54] Future spectroscopic analysis at low temperature can be helpful to resolve exciton behaviors of charge separation, especially for understanding the trap state ($\tau_5 > 10$ ns) in fundamental aspects.

CONCLUSIONS

Growth pathway for SSS ZnS nanowires is reported during structural investigation on SSS-catalyzed nanowires. Helical lattice orientation found in prenanowires is accompanied with ZB−WZ transformation, confirmed by HRTEM as well as synchrotron-based XRD, SAXS, and EXAFS. A three-step growth pathway is proposed as length growth (I), diameter thickening (II), and diameter ripening (III). The ZnS nanowires can be further engineered into cane-like heterostructures composed of ternary Ag_2S−CdS−ZnS semiconductors. Ensemble broadband emissions (450−800 nm) are qualitatively fitted with five excitonic lifetimes (τ_1 = 0.40 ± 0.12 ns, τ_2 = 4.38 ± 0.46 ns, τ_3 = 0.45 ± 0.05 ns, τ_4 = 2.03 ± 0.23 ns, and τ_5 = 11.16 ± 0.98 ns) for individual recombination pathways in the heterostructured nanowires. These nanowires under facile reaction conditions can be proposed to large-scale synthesis because of facile solution process, ambient environment, and mild temperature controls (120−200 °C).

https://dx.doi.org/10.1021/acsomega.0c02302
ACS Omega 2020, 5, 18441−18448

EXPERIMENTAL SECTION

Chemicals. Sulfur powder was purchased from Nihon Shiyaku. Cadmium acetate dihydrate (98%), and oleylamine (OLA, 80−90%) were obtained from Acrôs. Toluene and ethanol were obtained from ECHO. Silver acetate, sodium diethyldithiocarbamate trihydrate (NaDDTC), and zinc chloride (≥98%) were purchased from Sigma-Aldrich. All were used without further purification. Zinc diethyldithiocarbamate ($Zn(DDTC)_2$) and cadmium diethyldithiocarbamate ($Cd(DDTC)_2$) were synthesized at proper mole ratios of metallic salt (zinc chloride or cadmium acetate) to NaDDTC·$3H_2O$.

Synthesis of ZnS, CdS, and Heteronanowires. $Zn(DDTC)_2$ or $Cd(DDTC)_2$ was predissolved in OLA and then heated at target temperature (100−200 °C). Two ZnS nanowires (type-A and -B) were prepared according to recently developed SSS methods. For type-A ZnS nanowires, precursor $Zn(DDTC)_2$ (0.1 mmol) was dissolved in OLA (6 mL) and then heated to 120 °C (160, or 200 °C), followed by an injection of Ag(OAc) (25 mM in OLA, 200 μL) for nanowire growth at 120 °C (160, 200 °C) for 60 min. For type-B ZnS nanowires, the growth temperature was controlled at 160 °C for 15 min and then at 200 °C for another 15 min. Both ZnS nanowires can be used to synthesize CdS−ZnS heteronanowires. Sequential growth of CdS heterojunction was conducted by injecting the solution (20 mM in OLA, 200 μL) of $Cd(DDTC)_2$ precursor into ZnS nanowire solution at 100 °C. Aliquots of nanowire suspension after growth were purified with excess toluene and precipitated *via* centrifugation prior to structural and optical characterizations.

Characterizations and Instrumentation. Synchrotron-based SAXS was conducted at BL23A station at National Synchrotron Radiation Research Center (NSRRC) in Hsinchu, Taiwan. The incidence X-ray energy of 15 keV (0.83 Å) and the sample-to-detector distance of 2.80 m result in a q-range of 0.01−0.62 $Å^{-1}$ equivalent to the real-space distance of 62.8−1.013 nm. The scattering data extraction was performed using an X-ray scattering image analysis package (POLAR) installed in NSRRC. The EXAFS experiment was operated at 01C and 17C2 experiment station in NSRRC, with X-ray energy range = 6−33 keV with a resolution of 2.3×10^{-4}. The research was also conducted at experiment station BL12B2 (16 keV, λ = 0.775169 Å) in SPring-8, located in Harima Science Park City, Hyogo Prefecture, Japan. All EXAFS data were analyzed by FEFF7.0 to operate energy calibration and curve fitting. The XRD samples were all loaded in Hampton HR6-112 capillary with 0.5 mm in diameter and 80 mm in length. Synchrotron-based XRD investigation was conducted at experiment station TLS-BL01C2 (18 keV, λ = 0.68898 Å) and TPS-09A (15 keV, λ = 0.82656 Å) in NSRRC. The electron microscope images were obtained using Hitachi H-7100 (TEM) and FEI Tecnai G2 (HRTEM) located in the Instrumentation Center of National Taiwan University (NTU), Taipei, Taiwan. Spherical aberration-corrected field-emission STEM images were obtained using FEI Talos F200X, JEOL JEM-ARM200FTH and JEM-ARM200F, located in MA-TEK (http://www.ma-tek.com/en-global/), as well as the Instrumentation Center of National Tsing Hua University (NTHU) and National Chiao Tung University (NCTU), Hsinchu, Taiwan. Fluorescence lifetime measurement (Picoquant TimeHarp 300) and merged fluorescence images (Nikon TiE) were conducted in National Sun Yat-Sen University (NSYSU). The emission from the 607.5−682.5 nm bandpass filter (Chroma, ET645/75m) is more intense than the one from the 510/20 nm bandpass filter (Chroma, ET520/20m), matching the relative intensity of two emissions.

ASSOCIATED CONTENT

Supporting Information

The Supporting Information is available free of charge at https://pubs.acs.org/doi/10.1021/acsomega.0c02302.

Details of experimental results and more characterizations, including TEM, HRTEM, STEM, XRD, UV−vis, PL/PLE, SAXS, and EXAFS, for nanowires as well as precursor structure information (PDF)

AUTHOR INFORMATION

Corresponding Author

Yi-Hsin Liu − *Department of Chemistry, National Taiwan Normal University, Taipei 11677, Taiwan;* orcid.org/0000-0001-7069-4536; Email: yliu@ntnu.edu.tw

Authors

Ho-Ying Chen − *Department of Chemistry, National Taiwan Normal University, Taipei 11677, Taiwan*

Hsiu-Fang Fan − *Institute of Medical Science and Technology, National Sun Yat-Sen University, Kaohsiung 80424, Taiwan;* orcid.org/0000-0002-4870-351X

Yu-Hsien Chen − *Department of Chemistry, National Taiwan Normal University, Taipei 11677, Taiwan*

Fudong Wang − *Department of Chemistry, Washington University, Saint Louis, Missouri 63130, United States;* orcid.org/0000-0003-2914-1360

Complete contact information is available at: https://pubs.acs.org/10.1021/acsomega.0c02302

Funding

This research is supported by the Higher Education Sprout Project of National Taiwan Normal University (NTNU) and the Taiwan Ministry of Science and Technology (MOST) under contract nos. 105-2113-M-003-006-MY2, 107-2113-M-003-004 and 108-2113-M-003-008-MY2.

Notes

The authors declare no competing financial interest.

ACKNOWLEDGMENTS

We acknowledge staffs at National Synchrotron Radiation Research Center (NSRRC, Taiwan) for support and assistance in the following techniques. Powder XRD (BL01C2, TPS09A, Spring-8 12B2): Chung-Kai Chang, Yu-Chun Chuang, and Dr. Hwo-Shuenn Sheu; EXAFS (BL01C1, BL17C1): Dr. Ting-Shan Chan, Dr. Jyh-Fu Lee; SAXS (BL23A): Dr. Yi-Qi Yeh and Dr. U-Ser Jeng. Ching-Yen Lin, Ya-Yun Yang, and Ching-Wei Lu at the Precious Instrument Center of National Taiwan University for assistance with TEM and EA. Dr. Shieh at MA-TEK (Hsinchu, Taiwan) for HRTEM and STEM with HAADF−EDS mapping.

REFERENCES

(1) Pinion, C. W.; Christesen, J. D.; Cahoon, J. F. Understanding the vapor−liquid−solid mechanism of Si nanowire growth and doping to synthetically encode precise nanoscale morphology. *J. Mater. Chem. C* **2016**, *4*, 3890−3897.

(2) Yu, H. K.; Lee, J.-L. Growth mechanism of metal-oxide nanowires synthesized by electron beam evaporation: A self-catalytic vapor-liquid-solid process. *Sci. Rep.* **2015**, *4*, 6589.
(3) Li, S.; Huang, X.; Liu, Q.; Cao, X.; Huo, F.; Zhang, H.; Gan, C. L. Vapor-liquid-solid growth of endotaxial semiconductor nanowires. *Nano Lett.* **2012**, *12*, 5565.
(4) Suzuki, M.; Hidaka, Y.; Yanagida, T.; Klamchuen, A.; Kanai, M.; Kawai, T.; Kai, S. Essential role of catalyst in vapor-liquid-solid growth of compounds. *Phys. Rev. E: Stat., Nonlinear, Soft Matter Phys.* **2011**, *83*, 061606.
(5) Wu, Y.; Yang, P. Direct Observation of Vapor−Liquid−Solid Nanowire Growth. *J. Am. Chem. Soc.* **2001**, *123*, 3165−3166.
(6) Wang, Z.; Li, Z.; Kornowski, A.; Ma, X.; Myalitsin, A.; Mews, A. Solution-liquid-solid synthesis of semiconductor nanowires using clusters as single-source precursors. *Small* **2011**, *7*, 2464−2468.
(7) Wang, F.; Wayman, V. L.; Loomis, R. A.; Buhro, W. E. Solution-liquid-solid growth of semiconductor quantum-wire films. *ACS Nano* **2011**, *5*, 5188.
(8) Sun, J.; Buhro, W. E. The use of single-source precursors for the solution-liquid-solid growth of metal sulfide semiconductor nanowires. *Angew. Chem., Int. Ed. Engl.* **2008**, *47*, 3215.
(9) Dong, A.; Wang, F.; Daulton, T. L.; Buhro, W. E. Solution−Liquid−Solid (SLS) Growth of ZnSe−ZnTe Quantum Wires having Axial Heterojunctions. *Nano Lett.* **2007**, *7*, 1308.
(10) Wang, F.; Dong, A.; Sun, J.; Tang, R.; Yu, H.; Buhro, W. E. Solution−Liquid−Solid Growth of Semiconductor Nanowires. *Inorg. Chem.* **2006**, *45*, 7511.
(11) Zhang, L.; Yang, Q. Kinetic Growth of Ultralong Metastable Zincblende MnSe Nanowires Catalyzed by a Fast Ionic Conductor via a Solution-Solid-Solid Mechanism. *Nano Lett.* **2016**, *16*, 4008.
(12) Wang, F.; Buhro, W. E. Crystal-Phase Control by Solution-Solid-Solid Growth of II-VI Quantum Wires. *Nano Lett.* **2016**, *16*, 889.
(13) Wang, J.; Chen, K.; Gong, M.; Xu, B.; Yang, Q. Solution-solid-solid mechanism: superionic conductors catalyze nanowire growth. *Nano Lett.* **2013**, *13*, 3996.
(14) Sun, J.; Wang, L.-W.; Buhro, W. E. Synthesis of cadmium telluride quantum wires and the similarity of their effective band gaps to those of equidiameter cadmium telluride quantum dots. *J. Am. Chem. Soc.* **2008**, *130*, 7997−8005.
(15) Joyce, H. J.; Gao, Q.; Tan, H. H.; Jagadish, C.; Kim, Y.; Zhang, X.; Guo, Y.; Zou, J. Twin-Free Uniform Epitaxial GaAs Nanowires Grown by a Two-Temperature Process. *Nano Lett.* **2007**, *7*, 921−926.
(16) Sun, J.; Wang, L.-W.; Buhro, W. E. Synthesis of Cadmium Telluride Quantum Wires and the Similarity of Their Effective Band Gaps to Those of Equidiameter Cadmium Telluride Quantum Dots. *J. Am. Chem. Soc.* **2008**, *130*, 7997−8005.
(17) McNally, P. J. Techniques: 3D imaging of crystal defects. *Nature* **2013**, *496*, 37.
(18) Wang, J.; Yang, C.; Huang, Z.; Humphrey, M. G.; Jia, D.; You, T.; Chen, K.; Yang, Q.; Zhang, C. Seed-catalyzed heteroepitaxial growth and nonlinear optical properties of zinc selenide nanowires. *J. Mater. Chem.* **2012**, *22*, 10009.
(19) Dong, A.; Tang, R.; Buhro, W. E. Solution-based growth and structural characterization of homo- and heterobranched semiconductor nanowires. *J. Am. Chem. Soc.* **2007**, *129*, 12254.
(20) Wang, F.; Buhro, W. E. Role of Precursor-Conversion Chemistry in the Crystal-Phase Control of Catalytically Grown Colloidal Semiconductor Quantum Wires. *ACS Nano* **2017**, *11*, 12526−12535.
(21) Liu, Y.-H.; Wang, F.; Hoy, J.; Wayman, V. L.; Steinberg, L. K.; Loomis, R. A.; Buhro, W. E. Bright Core−Shell Semiconductor Quantum Wires. *J. Am. Chem. Soc.* **2012**, *134*, 18797−18803.
(22) Wang, J.; Fan, W.; Yang, J.; Da, Z.; Yang, X.; Chen, K.; Yu, H.; Cheng, X. Tetragonal−Orthorhombic−Cubic Phase Transitions in Ag2Se Nanocrystals. *Chem. Mater.* **2014**, *26*, 5647.
(23) Zhu, G.; Xu, Z. Controllable Growth of Semiconductor Heterostructures Mediated by Bifunctional Ag2S Nanocrystals as Catalyst or Source-Host. *J. Am. Chem. Soc.* **2011**, *133*, 148−157.
(24) Wu, P.-J.; Yu, J.-W.; Chao, H.-J.; Chang, J.-Y. Silver-Based Metal Sulfide Heterostructures: Synthetic Approaches, Characterization, and Application Prospects. *Chem. Mater.* **2014**, *26*, 3485−3494.
(25) O'Sullivan, C.; Gunning, R. D.; Sanyal, A.; Barrett, C. A.; Geaney, H.; Laffir, F. R.; Ahmed, S.; Ryan, K. M. Spontaneous room temperature elongation of CdS and Ag2S nanorods via oriented attachment. *J. Am. Chem. Soc.* **2009**, *131*, 12250−12257.
(26) Li, Q.; Zou, C.; Zhai, L.; Zhang, L.; Yang, Y.; Chen, X. a.; Huang, S. Synthesis of wurtzite CuInS2 nanowires by Ag2S-catalyzed growth. *CrystEngComm* **2013**, *15*, 1806−1813.
(27) Zou, C.; Li, M.; Zhang, L.; Yang, Y.; Li, Q.; Chen, X. a.; Xu, X.; Huang, S. Ag_2S-catalyzed growth of quaternary AgInZn7S9 semiconductor nanowires in solution. *CrystEngComm* **2011**, *13*, 3515−3520.
(28) Puthussery, J.; Kosel, T. H.; Kuno, M. Facile Synthesis and Size Control of II−VI Nanowires Using Bismuth Salts. *Small* **2009**, *5*, 1112−1116.
(29) Wang, F.; Richards, V. N.; Shields, S. P.; Buhro, W. E. Kinetics and Mechanisms of Aggregative Nanocrystal Growth. *Chem. Mater.* **2014**, *26*, 5−21.
(30) Wang, F.; Dong, A.; Buhro, W. E. Solution-Liquid-Solid Synthesis, Properties, and Applications of One-Dimensional Colloidal Semiconductor Nanorods and Nanowires. *Chem. Rev.* **2016**, *116*, 10888.
(31) Trindade, T.; O'Brien, P.; Pickett, N. L. Nanocrystalline Semiconductors: Synthesis, Properties, and Perspectives. *Chem. Mater.* **2001**, *13*, 3843−3858.
(32) Chen, R.; Li, D.; Liu, B.; Peng, Z.; Gurzadyan, G. G.; Xiong, Q.; Sun, H. Optical and excitonic properties of crystalline ZnS nanowires: toward efficient ultraviolet emission at room temperature. *Nano Lett.* **2010**, *10*, 4956−4961.
(33) Jehannin, M.; Rao, A.; Cölfen, H. New Horizons of Nonclassical Crystallization. *J. Am. Chem. Soc.* **2019**, *141*, 10120−10136.
(34) Zhang, Y.; Cai, J.; Ji, T.; Wu, Q.; Xu, Y.; Wang, X.; Sun, T.; Yang, L.; Hu, Z. Superionic conductor-mediated growth of ternary ZnCdS nanorods over a wide composition range. *Nano Res.* **2015**, *8*, 584.
(35) Hong, X.; Kim, J.; Shi, S.-F.; Zhang, Y.; Jin, C.; Sun, Y.; Tongay, S.; Wu, J.; Zhang, Y.; Wang, F. Ultrafast charge transfer in atomically thin MoS_2/WS_2 heterostructures. *Nat. Nanotechnol.* **2014**, *9*, 682−686.
(36) Wang, F.; Loomis, R. A.; Buhro, W. E. Spectroscopic Properties of Phase-Pure and Polytypic Colloidal Semiconductor Quantum Wires. *ACS Nano* **2016**, *10*, 9745−9754.
(37) Shah, S. H.; Azam, A.; Rafiq, M. A. Atomistic Simulations of CdS Morphologies. *Cryst. Growth Des.* **2015**, *15*, 1792−1800.
(38) Sun, J.; Buhro, W. E. The Use of Single-Source Precursors for the Solution−Liquid−Solid Growth of Metal Sulfide Semiconductor Nanowires. *Angew. Chem.* **2008**, *120*, 3259−3262.
(39) Zhang, L.; You, S.; Zuo, M.; Yang, Q. Solution Synthesis of Nonequilibrium Zincblende MnS Nanowires. *Inorg. Chem.* **2017**, *56*, 7679−7686.
(40) Li, D.; Nielsen, M. H.; Lee, J. R. I.; Frandsen, C.; Banfield, J. F.; De Yoreo, J. J. Direction-Specific Interactions Control Crystal Growth by Oriented Attachment. *Science* **2012**, *336*, 1014.
(41) Periwal, P.; Baron, T.; Gentile, P.; Salem, B.; Bassani, F. Growth strategies to control tapering in Ge nanowires. *APL Mater.* **2014**, *2*, 046105.
(42) Zhu, G.; Zhang, S.; Xu, Z.; Ma, J.; Shen, X. Ultrathin ZnS Single Crystal Nanowires: Controlled Synthesis and Room-Temperature Ferromagnetism Properties. *J. Am. Chem. Soc.* **2011**, *133*, 15605−15612.
(43) Ning, J.; Kershaw, S. V.; Rogach, A. L. Temperature-Controlled Fragmentation and Ripening: Synthesis of ZnSe Nanorods with Variable Dimensions and Crystal Structure Starting from Ultrathin ZnSe Nanowires. *Chem. Mater.* **2020**, *32*, 3960.

https://dx.doi.org/10.1021/acsomega.0c02302
ACS Omega 2020, 5, 18441−18448

(44) Pradhan, N.; Xu, H.; Peng, X. Colloidal CdSe Quantum Wires by Oriented Attachment. *Nano Lett.* **2006**, *6*, 720−724.
(45) Owen, J. The coordination chemistry of nanocrystal surfaces. *Science* **2015**, *347*, 615.
(46) Yao, W.-T.; Yu, S.-H.; Wu, Q.-S. From Mesostructured Wurtzite ZnS-Nanowire/Amine Nanocomposites to ZnS Nanowires Exhibiting Quantum Size Effects: A Mild-Solution Chemistry Approach. *Adv. Funct. Mater.* **2007**, *17*, 623−631.
(47) Csik, I.; Russo, S. P.; Mulvaney, P. Density Functional Study of Surface Passivation of Nonpolar Wurtzite CdSe Surfaces. *J. Phys. Chem. C* **2008**, *112*, 20413−20417.
(48) Rempel, J. Y.; Trout, B. L.; Bawendi, M. G.; Jensen, K. F. Density Functional Theory Study of Ligand Binding on CdSe (0001), $(000\bar{1})$, and $(11\bar{2}0)$ Single Crystal Relaxed and Reconstructed Surfaces: Implications for Nanocrystalline Growth. *J. Phys. Chem. B* **2006**, *110*, 18007−18016.
(49) Liu, Y.-H.; Wang, F.; Hoy, J.; Wayman, V. L.; Steinberg, L. K.; Loomis, R. A.; Buhro, W. E. Bright core-shell semiconductor quantum wires. *J. Am. Chem. Soc.* **2012**, *134*, 18797−18803.
(50) Steckel, J. S.; Zimmer, J. P.; Coe-Sullivan, S.; Stott, N. E.; Bulović, V.; Bawendi, M. G. Blue Luminescence from (CdS)ZnS Core-Shell Nanocrystals. *Angew. Chem., Int. Ed.* **2004**, *43*, 2154−2158.
(51) Demchenko, D. O.; Robinson, R. D.; Sadtler, B.; Erdonmez, C. K.; Alivisatos, A. P.; Wang, L.-W. Formation Mechanism and Properties of CdS-Ag_2S Nanorod Superlattices. *ACS Nano* **2008**, *2*, 627−636.
(52) Chiang, W.-H.; Mohan Sankaran, R. Linking catalyst composition to chirality distributions of as-grown single-walled carbon nanotubes by tuning Ni_xFe_{1-x} nanoparticles. *Nat. Mater.* **2009**, *8*, 882−886.
(53) Wayman, V. L.; Morrison, P. J.; Wang, F.; Tang, R.; Buhro, W. E.; Loomis, R. A. Bound 1D Excitons in Single CdSe Quantum Wires. *J. Phys. Chem. Lett.* **2012**, *3*, 2627−2632.
(54) Wheeler, D. A.; Zhang, J. Z. Exciton Dynamics in Semiconductor Nanocrystals. *Adv. Mater.* **2013**, *25*, 2878−2896.

https://dx.doi.org/10.1021/acsomega.0c02302
ACS Omega 2020, 5, 18441−18448